A&A 664, A100 (2022)
https://doi.org/10.1051/0004-6361/202243426

Astronomy & Astrophysics

Discovery of optical and infrared accretion disc wind signatures in the black hole candidate MAXI J1348–630

G. Panizo-Espinar[1,2], M. Armas Padilla[1,2], T. Muñoz-Darias[1,2], K. I. I. Koljonen[3,4,5], V. A. Cúneo[1,2], J. Sánchez-Sierras[1,2], D. Mata Sánchez[1,2], J. Casares[1,2], J. Corral-Santana[6], R. P. Fender[7,8], F. Jiménez-Ibarra[9], G. Ponti[10,11], D. Steeghs[12], and M. A. P. Torres[1,2]

[1] Instituto de Astrofísica de Canarias (IAC), Vía Láctea, La Laguna, 38205 Santa Cruz de Tenerife, Spain
e-mail: guayente.panizo@gmail.es
[2] Departamento de Astrofísica, Universidad de La Laguna, 38206 Santa Cruz de Tenerife, Spain
[3] Finnish Centre for Astronomy with ESO (FINCA), University of Turku, Väisäläntie 20, 21500 Piikkiö, Finland
[4] Aalto University Metsähovi Radio Observatory, PO Box 11000, 00076 Aalto, Finland
[5] Institutt for Fysikk, Norwegian University of Science and Technology, Trondheim, Norway
[6] European Southern Observatory, Alonso de Cordova 3107, Vitacura, Casilla 19001, Santiago, Chile
[7] Department of Physics, University of Oxford, Denys Wilkinson Building, Keble Road, Oxford OX1 3RH, UK
[8] Department of Astronomy, University of Cape Town, Private Bag X3, Rondebosch 7701, South Africa
[9] Australian Astronomical Optics, Macquarie University, 105 Delhi Rd, North Ryde, NSW 2113, Australia
[10] Osservatorio Astronomico di Brera, Via E. Bianchi 46, 23807 Merate (LC), Italy
[11] Max-Planck-Institut fur Extraterrestrische Physik, Giessenbachstrasse, 85748 Garching, Germany
[12] Department of Physics, University of Warwick, Coventry CV4 7AL, UK

Received 25 February 2022 / Accepted 26 May 2022

ABSTRACT

MAXI J1348–630 is a low mass X-ray binary discovered in 2019 during a bright outburst. During this event, the system experienced both hard and soft states following the standard evolution. We present multi-epoch optical and near-infrared spectroscopy obtained with X-shooter at the Very Large Telescope. Our dataset includes spectra taken during the brightest phases of the outburst as well as the decay towards quiescence. We study the evolution of the main emission lines, paying special attention to the presence of features commonly associated with accretion disc winds, such as blueshifted absorptions, broad emission line wings and flat-top profiles. We find broad emission line wings in Hα during the hard-to-soft transition and blueshifted absorption troughs at $\sim$−500 km s^{-1} in Hβ, He I–5876, Hα and Paβ during the bright soft-intermediate state. In addition, flat-top profiles are seen throughout the outburst. We interpret these observables as signatures of a cold (i.e., optical-to-infrared) accretion disc wind present in the system. We discuss the properties of the wind and compare them with those seen in other X-ray transients. In particular, the wind velocity that we observe is low when compared to those of other systems, which might be a direct consequence of the relatively low binary inclination, as suggested by several observables. This study strengthens the hypothesis that cold winds are a common feature in low mass X-ray binaries and that they can also be detected in low inclination objects via high-quality optical and infrared spectroscopy.

Key words. accretion, accretion disks – binaries: close – stars: winds, outflows – X-rays: binaries – stars: individual: MAXI J1348−630

1. Introduction

Low mass X-ray binaries (LMXBs) are binary systems comprising a stellar-mass black hole (BH) or a neutron star (NS) that is accreting gas from a low mass donor star ($\lesssim$1 $M_\odot$). The infalling material forms an accretion disc around the compact object (Shakura & Sunyaev 1973), whose internal regions reach temperatures high enough (10^6–10^7 K) to emit in X-rays. The vast majority of LMXBs are transients. They spend most of their lives in a quiescent, low-luminosity state, showing occasional accretion episodes when their luminosity increases by several orders of magnitude: the so-called outbursts.

During outbursts, LMXBs usually evolve following a common X-ray hysteresis pattern (e.g., Muñoz-Darias et al. 2014) that is related to their accretion properties. At the beginning of the outburst, the X-ray spectrum is dominated by a hard, power-law component thought to be produced by inverse-Compton processes in a corona of hot electrons (e.g., Gilfanov 2010). This state is known as the hard state. As the outburst continues the system enters the soft state, when the spectrum becomes dominated by a soft, thermal component arising in the accretion disc. Low mass X-ray binaries can also be found in intermediate states, when they are transitioning between the above two main states (see e.g., McClintock & Remillard 2006; Done et al. 2007; Belloni et al. 2011).

Outbursts are also characterised by the presence of outflows, with observational evidence indicating that they are directly correlated with the accretion state (for a review, see e.g., Fender & Muñoz-Darias 2016). These outflows are usually observed in two flavours: jets and winds. Radio jets are ubiquitously observed in the hard (compact jet) and intermediate (discrete ejections) states, but not during the soft state (e.g., Gallo et al. 2003; Fender et al. 2004; Russell et al. 2011). Conversely, hot X-ray winds are mainly detected during the

Table 1. Summary of the observing campaign.

Epoch	2019 Date (MJD)	X-ray state	r-band (i-band) [a] (AB magnitude)	Total exposure time (s)/Slit width ($''$)		
				UVB	VIS	NIR
1	06 Feb. (58520)	Hard-intermediate	15.4	2200/1.3	2000/1.2	2200/1.2
2	10 Feb. (58524)	Soft-intermediate	15.4	4524/1.3, 1.0	4116/1.2, 0.9	3360/1.2, 0.9
3	11 Feb. (58525)	Soft-intermediate	15.5	2324/1.0	2216/0.9	1160/0.9
4	15 Feb. (58529)	Soft-intermediate	15.6	2324/1.0	2216/0.9	1160/0.9
5	18 Feb. (58532)	Soft-intermediate	15.6	3924/1.9, 1.0	3416/1.2, 0.9	2760/1.2, 0.9
6	24 Feb. (58538)	Soft-intermediate	–	1600/1.3	1200/1.2	1600/1.2
7	06 Mar. (58543)	Soft	–	2220/1.3	2000/1.2	2200/1.2
8	08 Mar. (58550)	Soft	16.2 (15.1)	2220/1.3	2000/1.2	2200/1.2
9	09 Mar. (58551)	Soft	15.9	2324/1.0	2216/0.9	1160/0.9
10	19 Mar. (58561)	Soft	–	2200/1.3	2000/1.2	2200/1.2
11	03 May (58606)	Hard	–	1920/1.3	2036/1.2	1920/1.2
12	05 May (58608)	Hard	(16.9)	1920/1.3	2036/1.2	1920/1.2

Notes. [a]The estimated uncertainty is ∼0.07 and ∼0.03 in r-band and i-band, respectively.

soft state as blueshifted X-ray absorptions in spectral transitions of highly ionised material, such as Fe XXV and Fe XXVI (Ueda et al. 1998; Neilsen & Lee 2009; Ponti et al. 2012, 2014; Díaz Trigo & Boirin 2016). In addition, more recent studies have also shown the presence of colder accretion disc winds, which are mainly observed in optical emission lines and can be simultaneous with the jet (e.g., Muñoz-Darias et al. 2016). These are revealed by some specific signatures: blueshifted absorptions (P-Cygni profiles or absorption troughs), broad emission line wings, flat-top line profiles, and line asymmetries. To date, they have been seen in a handful of BH (e.g., Muñoz-Darias et al. 2016, 2018, 2019; Cúneo et al. 2020b; Mata Sánchez et al. 2022) and NS transients (e.g., Muñoz-Darias et al. 2020; see also Castro Segura et al. 2022 for a detection in the ultraviolet). Furthermore, near-infrared studies show that these lower ionisation winds, also known as cold winds, are likely active during most of the outburst (Sánchez-Sierras & Muñoz-Darias 2020). Interestingly, both X-ray and optical-to-infrared (OIR) wind detections occurred in systems with relatively high orbital inclinations, which is commonly interpreted as the wind having an equatorial geometry (e.g., Ponti et al. 2012; but see Higginbottom et al. 2019).

MAXI J1348–630 (J1348 hereafter) is a new LMXB, discovered during an outburst episode on 2019 January 26 (Yatabe et al. 2019) by the Monitor of All-sky X-ray Image (MAXI) nova alert system (Matsuoka et al. 2009). The peak X-ray flux was measured on February 10 ($\sim 1.0 \times 10^{-7}$ erg cm^{-2} s^{-1}; Lamer et al. 2021; Carotenuto et al. 2021), and the highest reported optical flux ($g' = 16.1$) was measured on February 5 (Baglio et al. 2019). A hard-to-soft transition began on February 3 (Nakahira et al. 2019). X-ray studies using the Neutron Star Interior Composition Explorer (NICER) revealed type-B quasi-periodic oscillations between February 8 and 26 (Belloni et al. 2020; Zhang et al. 2021, 2022), associated with the soft-intermediate state (SIMS). The main outburst lasted ∼3 months and was followed by a few hard-state-only re-brightenings (Russell et al. 2019b; Pirbhoy et al. 2020; Negoro et al. 2020; Baglio et al. 2020; Zhang et al. 2020; Corral-Santana et al. 2016; see also Cúneo et al. 2020a). This transient is estimated to be at ∼2–3 kpc (Chauhan et al. 2021; Russell et al. 2019a; Lamer et al. 2021) and has been suggested to harbour a BH, based on its spectral and timing properties (Sanna et al. 2019; Belloni et al. 2020; Zhang et al. 2020).

In this paper we present multi-epoch spectroscopy of J1348 obtained with X-shooter at the Very Large Telescope (VLT), which covers ultraviolet, optical, and near-infrared wavelengths. We study the presence or absence of the most typical LMXB emission lines, as well as the evolution of their main properties.

2. Observations and data reduction

A total of 12 epochs of spectroscopy were obtained between February and May 2019 with X-shooter (Vernet et al. 2011) at the VLT-UT2 in Cerro Paranal, Chile. We obtained photometric magnitudes for the epochs with available acquisition images, which are presented in the observing log (Table 1). Each spectral observation included 4–16 exposures in nodding configuration with total exposure times of 1100–4500 s and covering from 3000 to 25 000 Å between the three arms of the instrument. We used slit widths of 1.0″–1.3″, 0.9″–1.2″, and 0.9″–1.2″ for the ultraviolet (UVB), visible (VIS), and infrared (NIR) arms, producing velocity resolutions of ∼55–73, ∼34–46, and ∼53–70 km s^{-1}, respectively. Airmasses ranged from 1.28 to 1.95.

The spectra were reduced using the X-shooter ESO Pipeline v3.3.5. Flux calibration standard stars in epochs #3–5 and #8–9 were not bright enough in the infrared. Therefore, those spectra were calibrated with the standard star from epoch #10. Atmospheric telluric absorptions in optical and infrared ranges were corrected using MOLECFIT (Smette et al. 2015; Kausch et al. 2015), and the continuum adjacent to each spectral line of interest was individually normalised for a detailed study.

3. Analysis and results

J1348 was first detected on 2019 January 26 (MJD 58509) and it was X-ray active for ∼100 days. The upper panel of Fig. 1 shows its X-ray light curve, which follows the usual fast rise (∼10 days) and a slower decay towards quiescence. The lower panel in Fig. 1 shows the hardness-intensity diagram (HID; Homan et al. 2001) of daily averaged count rates from MAXI, where the X-ray colour is defined as the ratio between hard (4–20 keV) and soft (2–4 keV) count rates. The source displays the characteristic hysteresis pattern commonly observed in LMXBs during outbursts (Muñoz-Darias et al. 2014). According to this diagram, we consider epoch #1 to be in the hard-to-soft transition (most likely in the hard-intermediate state),

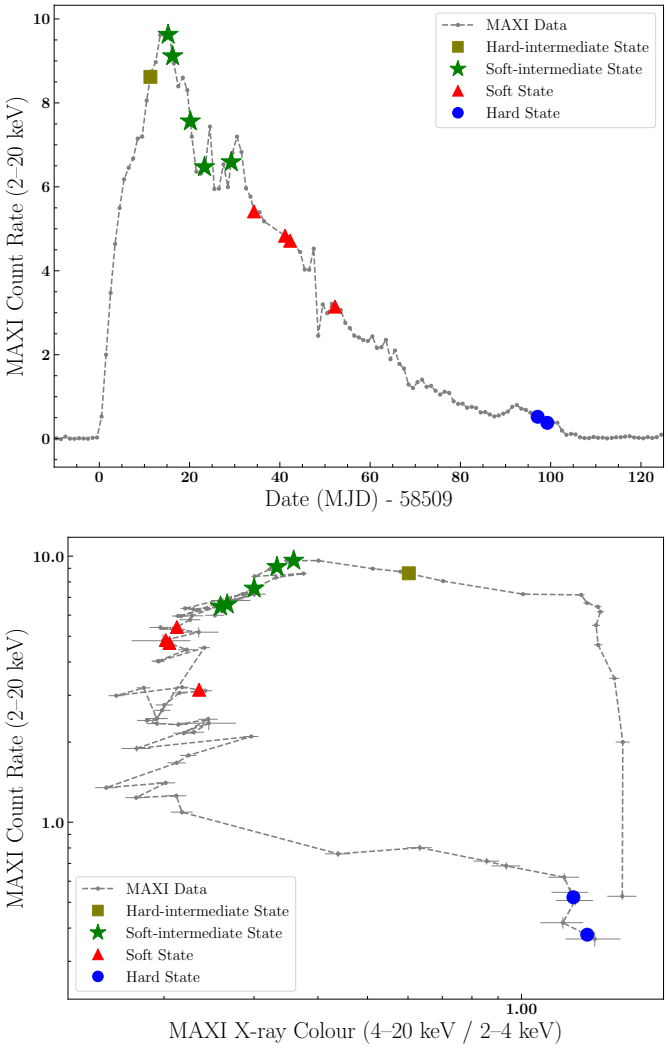

Fig. 1. Light curve (*upper panel*) and HID (*lower panel*) of J1348 during its 2019 outburst (MAXI data between MJD 58509 and 58634). The small grey dots represent X-ray data, and the coloured symbols mark the interpolated position for each X-shooter epoch. For the HID we only considered data with count rates exceeding 0.025 photons cm^{-2} s^{-1} in each band. The X-ray colour is defined as the ratio between the hard (4–20 keV) and the soft (2–4 keV) count rates. The source displays the classic hysteresis loop in the anticlockwise direction.

#2–6 in the SIMS (type-B quasi-periodic oscillations reported in Belloni et al. 2020; Zhang et al. 2020), #7–10 in the soft state, and #11–12 in the low-luminosity hard state; in this last phase, the source was returning to quiescence. A summary of the observations and associated X-ray states is shown in Table 1.

3.1. Spectral evolution

The OIR spectrum of J1348 varied as the outburst evolved, with the most prominent emission lines observed during the last epochs (i.e., hard states; epochs #11–12). We observed several hydrogen emission lines in the broad spectral range covered, from the Balmer, Paschen, and Brackett series (as an example, see epoch #5 spectra in Fig. 2). Helium lines such as He II at 4686 Å (He II–4686), He I–5876, He I–6678, and He I–10830 are also visible. Figure 3 shows the evolution of the main emission lines across the observing campaign. All of them were individually normalised by fitting a first-order polynomial to their local continuum with the emission line masked (and the underlying absorption also masked in Balmer lines).

The Hα line shows intense, double-peaked profiles in many epochs. The peak-to-peak separation increases as the outburst evolves, from 310 ± 150 km s^{-1} in epoch #1 to a maximum of 600 ± 70 km s^{-1} in the last epoch. This behaviour, revealed by two-Gaussian models fitted to the line (with all parameters free to vary), has been observed in other systems and interpreted as an indication of the disc shrinking towards the end of the outburst (e.g., Casares et al. 2019; Mata-Sánchez et al. 2015a; Torres et al. 2015; Corral-Santana et al. 2013). This line shows an asymmetric profile and broad wings reaching $\sim\pm1500$ km s^{-1} in epoch #1 (see Figs. 3 and 4), while a flat-top profile is visible in epoch #6. An underlying broad absorption component (from $\sim$–2000 to $\sim$1700 km s^{-1}) is also present during most epochs, a feature that is relatively commonly observed in LMXBs in outburst (Soria et al. 2000; Casares et al. 1995; Yao et al. 2021). This is also present in Hβ and Hγ (see e.g., Fig. 2).

The Hβ line shows emission profiles similar to those of Hα, although much less intense. This line also shows broad absorptions in every epoch, and they are particularly clear in epochs #5–12 ($\sim$10% below the continuum, reaching $\sim\pm3000$ km s^{-1}). This specially prominent and redshifted absorption has been observed in other transients in outburst (e.g., Cúneo et al. 2020b) and is most likely a combination of the aforementioned Balmer broad absorption component and an additional contribution from a broad diffuse interstellar band (DIB) at $\sim$4882 Å with a full width at half maximum of $\sim$20 Å (e.g., Kaur et al. 2012; Jenniskens & Désert 1994; Buxton & Vennes 2003).

The Paβ profiles are qualitatively similar, but broader and less intense than the Hα profiles. In addition, several lines from the Paschen series show flat-top-like profiles in epochs #4, #6, and #9. Similar boxy line profiles are also observed in high-order Brackett lines during epochs #2 and #4 (e.g., Br-10, 11, and 12, which are similar to those seen in other transitions; see Fig. 3). The Brγ line shows profiles similar to those of Paβ (Fig. 3) except for the less prominent ones in the harder epochs (#1, #11–12), as observed in other transients (Sánchez-Sierras & Muñoz-Darias 2020).

Finally, He I–10830 is generally the most intense He line. It shows line profiles very similar to those of Hα, but with more prominent double peaks. Its peak-to-peak separation also increases as the outburst evolves, from 400 ± 60 km s^{-1} to a maximum of 590 ± 90 km s^{-1} in epoch #12. Other typical He lines, such as He I–5876 and He II–4686, are also visible. The latter, which is expected to trace hotter (inner) gas, shows boxy or double-peaked profiles (characteristic of gas rotating in an accretion disc; e.g., Smak 1969) depending on the epoch (see Fig. 3).

3.2. Outflow features: blueshifted absorption troughs and broad wings

As mentioned above, during some stages of the outburst several spectral lines display features that could be interpreted as signatures of accretion disc winds. These include blueshifted absorptions, broad emission line wings, and line profiles with asymmetries or flat tops. Figures 3 and 4 show the presence of a blueshifted absorption trough centred at -500 km s^{-1} in epochs #2 and #6 in Hβ, He I–5876, Hα, and Paβ (dashed-dotted red line). In the first three cases, this feature resembles the blueshifted absorption of a P-Cygni profile. However, due to the broader profile of Paβ, the absorption trough is observed as a dent on its blue wing. Figure 5 shows that this feature is not

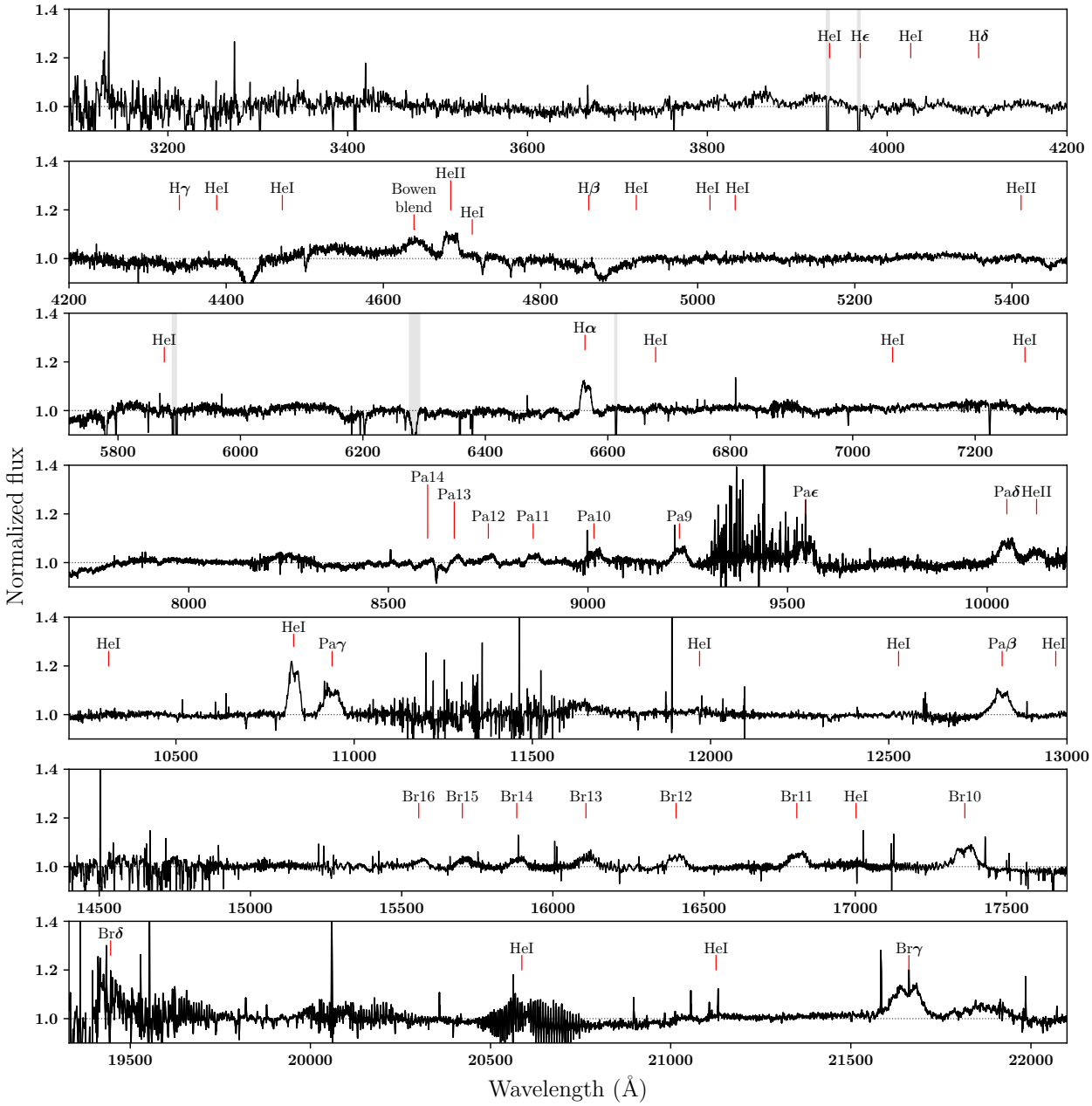

Fig. 2. Normalised OIR spectrum during epoch #5. Relevant emission lines are labelled, and prominent DIBs are shaded in grey.

visible in Paγ nor Brγ. It is worth noting that the blueshifted absorption becomes visible again in the soft state (epoch #10), but in this case only in Paβ (see Fig. 4). Interestingly, the profile of Paβ in epochs #2 and #6 also suggests the presence of an underlying broader emission component, whose blue wing reaches $\sim -1700\,\mathrm{km\,s^{-1}}$ (blue vertical dashed line in Figs. 3–5) and the red one $\sim +1000\,\mathrm{km\,s^{-1}}$. This velocity is similar to that of the aforementioned broad absorption components best seen in Hα in epoch #1 ($\sim \pm 1700\,\mathrm{km\,s^{-1}}$; see Fig. 5).

3.3. The excesses diagnostic diagram

Some of the spectral features revealed by visual inspection suggest the presence of an outflow in the system (see above). In a second step, we performed a systematical inspection using the excesses diagnostic diagram. This tool was introduced by Mata Sánchez et al. (2018) and is based on studying the deviation of the spectral line wings from a pure Gaussian profile. The coordinates of each epoch in the diagram are the so-called red and blue excesses (EW_{r+} and EW_{b-}), defined as the equivalent width (EW) of the line wings after subtracting the Gaussian model (see Muñoz-Darias et al. 2019; Panizo-Espinar et al. 2021 for details). Thus, an epoch with a P-Cygni profile (i.e., red emission and blue absorption, thus $\mathrm{EW}_{r+} > 0$ and $\mathrm{EW}_{b-} < 0$) would lie in the bottom-right quadrant, while broad wings would make it fall in the top-right one (i.e., red and blue emission, $\mathrm{EW}_{r+} > 0$ and $\mathrm{EW}_{b-} > 0$).

Although this method is generally applied to Hα, in this case the results are inconclusive due to the variable contamination by the underlying broad absorption component. We tried a multi-Gaussian fitting to model the broad absorption, but it did not provide meaningful results. The Paβ line, on the other hand, shows significant ($>5\sigma$), positive red and blue wing residuals during epoch #2, measured in the $(\pm)700$–$1500\,\mathrm{km\,s^{-1}}$ velocity bands

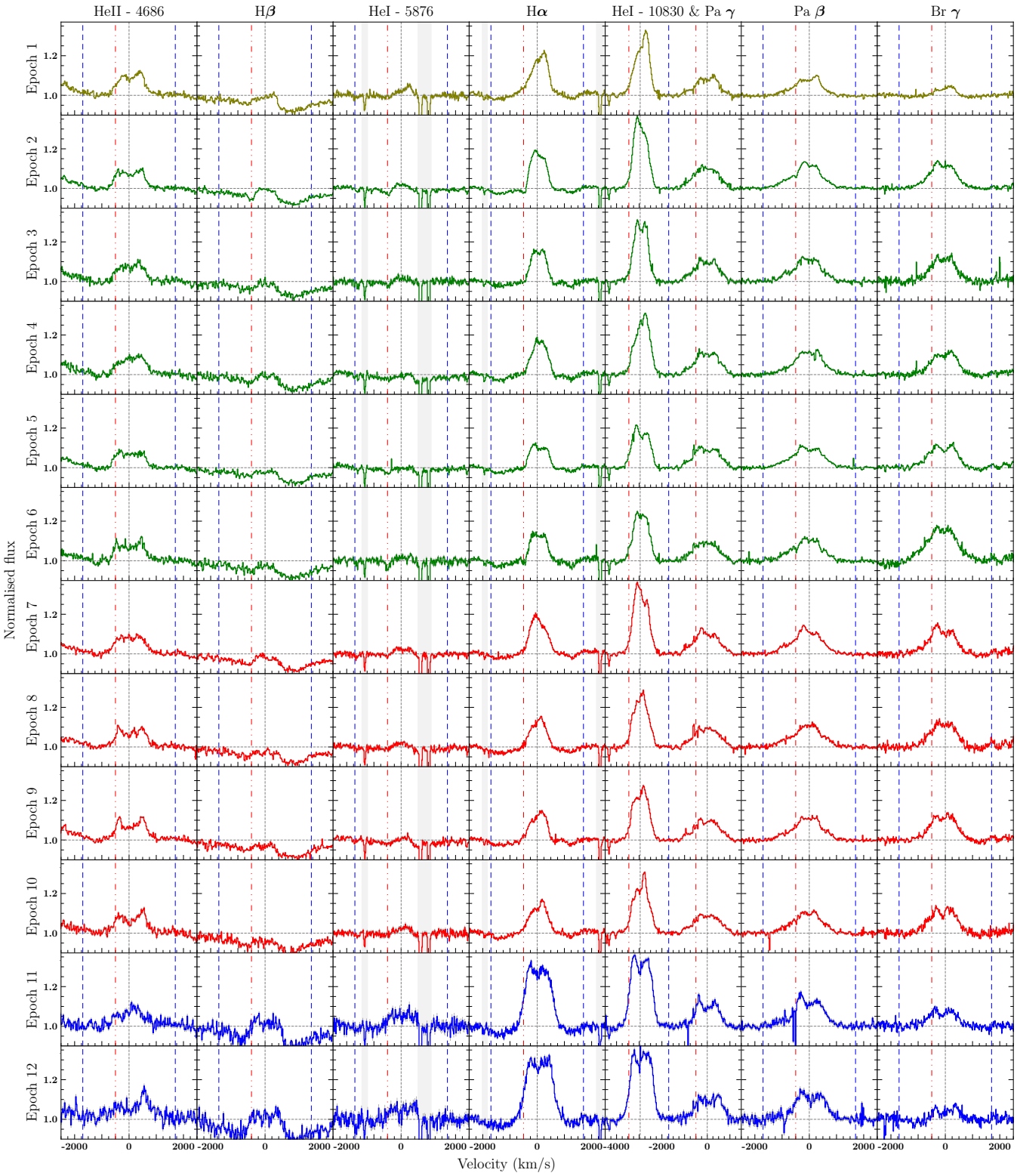

Fig. 3. Evolution of the most relevant emission lines. The colour code is the same as in Fig. 1. The vertical dashed blue and dashed-dotted red lines mark $\pm 1700\,\mathrm{km\,s^{-1}}$ and $-500\,\mathrm{km\,s^{-1}}$, velocities of the blue wing and the absorption trough of Paβ, respectively (in epochs #2 and #6). Grey bands indicate regions contaminated by DIBs or tellurics. The emission at $-2500\,\mathrm{km\,s^{-1}}$ in the He II–4686 column is produced by the Bowen blend.

(Fig. 6). This is consistent with the presence of broad wings, as suggested by the visual inspection. No P-Cygni profiles are revealed by the diagram, which is an expected outcome given that the blueshifted absorptions appear as small dents (with small EWs) on Paβ (see Sect. 3.2).

4. Discussion

We have presented OIR spectroscopy of J1348 during its 2019 discovery outburst. We studied the evolution of the main spectral lines throughout the entire accretion episode, paying special

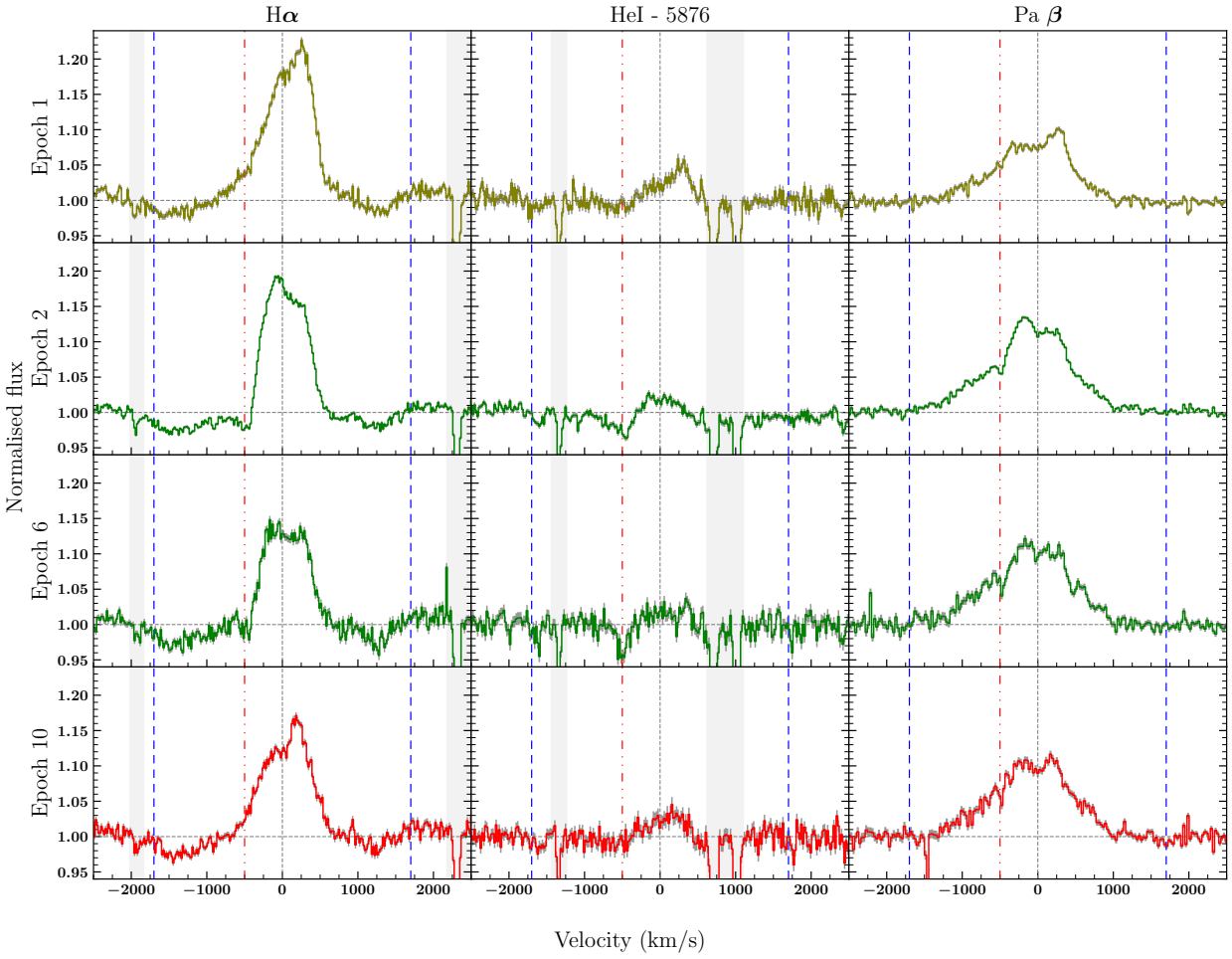

Fig. 4. Hα, He I–5876, and Paβ profiles in epochs #1, 2, 6, and 10 (re-binned by a factor of two). Vertical lines and colours have the same meanings as in previous figures.

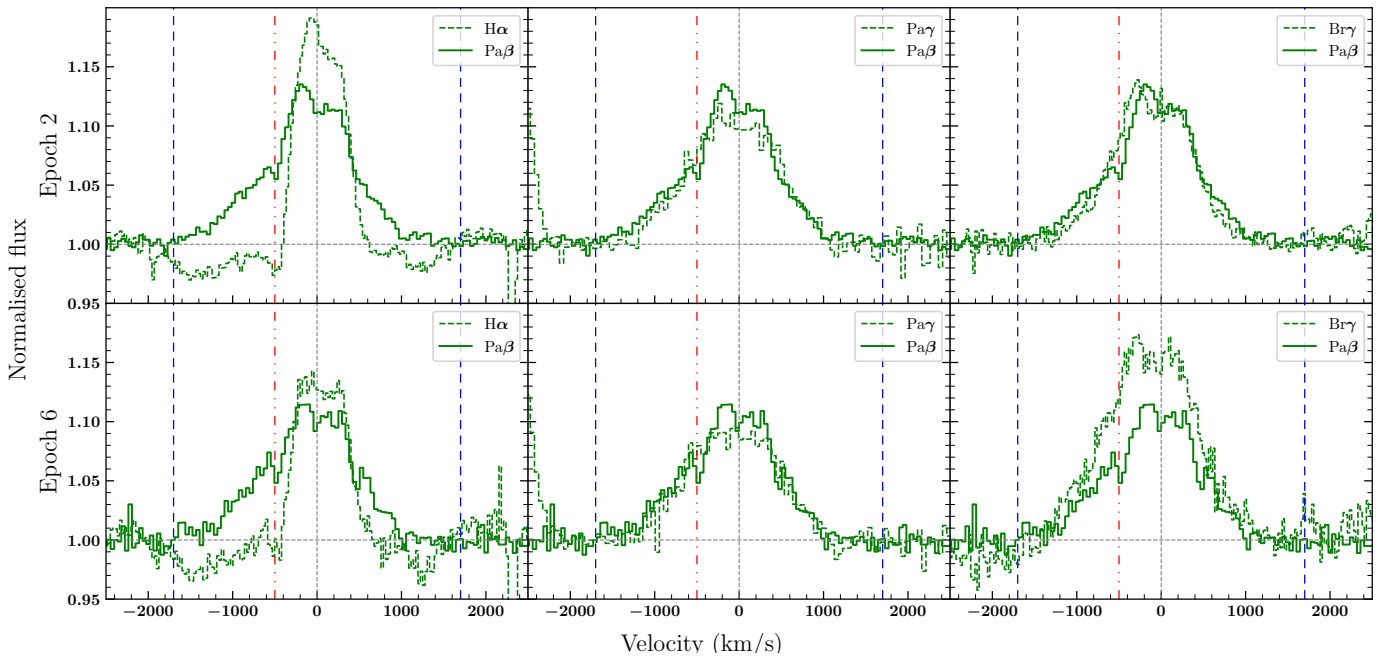

Fig. 5. Paβ profiles (solid line) compared to Hα, Paγ, and Brγ (dashed line) in epochs #2 (*upper panel*) and #6 (*lower panel*). Spectral lines are re-binned by a factor of three for clarity. Vertical lines and colours have the same meaning as in previous figures.

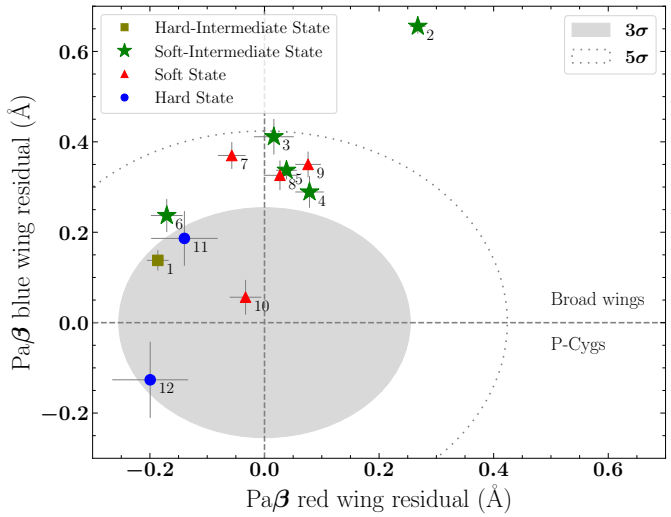

Fig. 6. Paβ excesses diagnostic diagram. Symbols and colour codes have the same meanings as in Fig. 1. The grey region and dotted line indicate the 3σ and 5σ contours, respectively. Epochs showing wind-related signatures are expected to lie in the right quadrants.

attention to those particularly sensitive to outflows. We find several spectral features commonly associated with the presence of an accretion disc wind.

Firstly, a blueshifted absorption trough is seen at $-500\,\mathrm{km\,s^{-1}}$ during the bright SIMS (epoch #2 and #6) in Hβ, He I–5876, Hα, and Paβ (see Figs. 4 and 5). The fact that this narrow feature is simultaneously observed at the same velocity in four different lines rules it out as an artefact (e.g. deficient sky subtraction) or as having a DIB origin. This absorption at $-500\,\mathrm{km\,s^{-1}}$ is present again in Paβ during the soft state (epoch #10; see Fig. 4).

Secondly, broad emission line wings are spotted in Hα during epoch #1, reaching $\sim\pm1500\,\mathrm{km\,s^{-1}}$, and in Pa$\beta$ during epoch #2, reaching $\sim-1700\,\mathrm{km\,s^{-1}}$ (see Fig. 4 and Sect. 3.3). Profiles with broad wings can be interpreted as signatures of outflows (e.g., Muñoz-Darias et al. 2018; Panizo-Espinar et al. 2021; see also Prinja et al. 1996 for winds in massive stars).

Finally, several Balmer and helium lines, such as Hα, He I–5876, and He I–10830, are asymmetric with a negative skew (i.e., the emission peak appears redshifted compared to the rest wavelength) in epoch #1 (hard-intermediate state; Fig. 3). Similar profiles are commonly seen in systems that show conspicuous signatures of outflows (e.g., Muñoz-Darias et al. 2019).

Additionally, flat-top profiles are observed in epoch #2 in several hydrogen lines of the Paschen and Brackett series (Paγ, Paδ, Pa-9, Pa-10, Pa-11, Br-10, and Br-11), in epoch #6 in Hα, Paschen, and helium lines (He I–5876 and He I–10830), and epochs #9–10 in Paschen and Brackett series (see Fig. 3), suggesting the presence of the wind through the soft state. These profiles are also present (albeit with a weak central absorption) in the Balmer series and He I lines during the final hard state epochs, #11–12 (Fig. 3). Similar features are commonly detected in novae and Wolf-Rayet stars (Beals 1931; Vainu Bappu & Menzel 1954; Williams & Mason 2010) and are generally understood as a signature of expanding envelopes (i.e., outflows; e.g., Soria et al. 2000).

Overall, at least four different wind-related spectral features are visible in J1348: blueshifted absorption troughs, broad emission line wings, asymmetries, and flat-top profiles, some of which appear simultaneously in several spectral lines. We interpret these features as evidence of an OIR accretion disc wind present during most of the brightest phase of the outburst. Unfortunately, we note that we were not able to monitor the system during the initial hard state, and in particular during the hard state peak, a stage in which other systems have shown the most conspicuous optical wind signatures (e.g., MAXI J1820+070, Muñoz-Darias et al. 2019; GRS 1716−249, Cúneo et al. 2020a; MAXI J1803−298, Mata Sánchez et al. 2022). We also note that the possible presence of accretion disc winds in J1348 during previous activity phases of the system would support the hypothesis of them contributing to create a low density cavity in which the system seems to be embedded (Carotenuto et al. 2021), as suggested by other authors (Carotenuto et al. 2022).

4.1. Comparison with other systems

As summarised in Table 2, OIR accretion disc winds have been detected in a number of LMXBs during outbursts. Most cases are BH transients with conspicuous wind features present during the hard state, although there are also examples of OIR winds found in NS systems (Bandyopadhyay et al. 1999; Muñoz-Darias et al. 2020). In particular, most detections correspond to P-Cygni profiles observed in high inclination (>60°) sources, with blue-edge velocities indicating relatively high velocity outflows (1200–3000 $\mathrm{km\,s^{-1}}$). This prototypical wind signature is not particularly obvious in our dataset. However, we find weak, blueshifted absorption troughs in several lines in epochs #2 and #6. In particular, the blue-edge velocity of this absorption in He I–5876 points to a terminal velocity of $\sim900\,\mathrm{km\,s^{-1}}$, lower than the OIR wind velocities measured in other LMXBs (Table 2). There are also other (somewhat more tentative) wind features (e.g., broad emission line wings in Rahoui et al. 2014; Soria et al. 2000; Panizo-Espinar et al. 2021), which typically reach higher velocities than those inferred from the P-Cygni profiles (see e.g., Muñoz-Darias et al. 2018, 2019). This is also the case for J1348, where the emission line wings of Hα reach considerably higher values ($\sim1500\,\mathrm{km\,s^{-1}}$) than the narrow, blueshifted absorptions (500–900 $\mathrm{km\,s^{-1}}$). This might be explained by a dissimilar dependence of the various wind signatures on the orbital inclination, with blueshifted absorptions being particularly sensitive to the presence of outflowing material along the line-of-sight (see Sect. 4).

Among the systems in Table 2, the comparison with MAXI J1820+070 is particularly relevant. This BH transient showed a variety of wind signatures during its 2018 outburst, which also followed a standard evolution with hard and soft states. Specifically, Paβ and Paγ showed absorption troughs with kinetic properties (wind velocity of 1200–2000 $\mathrm{km\,s^{-1}}$) similar to those derived from P-Cygni profiles present in other spectral lines (Sánchez-Sierras & Muñoz-Darias 2020). This is consistent with the behaviour of J1348, where the absorption features in Paβ indicate the same velocity as those found in Hα and He I–5876.

4.2. On the state dependence of the wind features

The comparison of J1348 with other LMXBs allows us to revisit the state dependence of the wind-related OIR features. In J1348, the most compelling evidence for winds is arguably found during the SIMS, while the strongest optical winds are usually found at the hard state peak. A possible exception would be the first soft observation of MAXI J1820+070 (Muñoz-Darias et al. 2019), which was obtained right after the hard-to-soft transition (i.e., similar to epoch #2 in this paper).

Our observations did not cover the bright hard state. Nonetheless, additional OIR wind features were observed

Table 2. Characteristics of LMXBs with OIR winds and properties of the outflow.

(a) OIR wind detections							
LMXB	Object	i (°)	P (h)	Wind features	Vel. (km s^{-1}) [(a)]	Spectral range	References
GX13+1	NS	60–80	589	P-Cygni	~2400	NIR	1, 1b, 1c, 1d
V404 Cyg	BH	60–70	155.3	P-Cygni	1500–3000	Optical	2, 2b, 2c, 2d, 2e
				Broad wings	~3000		
V4641 Sgr	BH	60–70	67.6	P-Cygni	900–1600	Optical	3, 3b, 3c, 3d, 3e
				Broad wings	~3000		
Swift J1357.2−0933	BH	≳80	2.8	P-Cygni	1600–4000	Optical	4, 4b, 4c
MAXI J1820+070	BH	67–81	16.4	P-Cygni	1200–1800	Optical	5, 5b, 5c, 5d
				Broad wings	~1800	Optical	
				Blueshifted abs. [(b)]	1200–1800	NIR	
Swift J1858.6−0814	NS	Dipping/eclipsing	21.8	P-Cygni	1700–2400	Optical	6, 6b, 6c
GRS1716-249	BH	?	?	P-Cygni	~2000	Optical	7
				Flat-top, asymmetries	–		
MAXI J1803–298	BH	Dipping	7–8	P-Cygni	~1250	Optical	8, 8b, 8c
MAXI J1348–630	BH	Mid-to-low	?	Broad wings	1500–1700	Optical, NIR	this work, 9
				Blueshifted abs.	500–900	Optical, NIR	
				Flat-top, asymmetries	–	Optical, NIR	
(b) Tentative OIR wind detections							
LMXB	Object	i (°)	P (h)	Wind features	Vel. (km s^{-1}) [(a)]	Spectral range	References
Sco X-1	NS	< 40	18.9	P-Cygni	~2600	NIR	1, 10, 10b, 10c
GRO J1655–40	BH	67–70	62.9	Flat-top, asymmetries	–	Optical	11, 11b, 11c
GX339–4	BH	37–78	42.2	Broad wings	?	NIR	12, 12b
Aql X-1	NS	23–53	18.7	Broad wings	800	Optical	13, 13b, 13c

Notes. [(a)]Terminal velocity. [(b)]Absorption.
References. (1) Bandyopadhyay et al. (1999); (1b) Iaria et al. (2014); (1c) Díaz Trigo et al. (2012); (1d) Homan et al. (2016); (2) Muñoz-Darias et al. (2016); (2b) Muñoz-Darias et al. (2017); (2c) Mata Sánchez et al. (2018); (2d) Casares et al. (1991); (2e) Khargharia et al. (2010); (3) Muñoz-Darias et al. (2018); (3b) Lindstrøm et al. (2005); (3c) Chaty et al. (2003); (3d) Orosz et al. (2001); (3e) Macdonald et al. (2014); (4) Jiménez-Ibarra et al. (2019); (4b) Mata-Sánchez et al. (2015a); (4c) Corral-Santana et al. (2013); (5) Muñoz-Darias et al. (2019); (5b) Sánchez-Sierras & Muñoz-Darias (2020); (5c) Torres et al. (2019); (5d) Torres et al. (2020); (6) Muñoz-Darias et al. (2020); (6b) Buisson et al. (2020); (6c) Buisson et al. (2021); (7) Cúneo et al. (2020b); (8) Mata Sánchez et al. (2022); (8b) Homan et al. (2021); (8c) Xu et al. (2021); (9) Carotenuto et al. (2022); (10) Fomalont et al. (2001); (10b) Gottlieb et al. (1975); (10c) Mata Sánchez et al. (2015b); (11) Soria et al. (2000); (11b) van der Hooft et al. (1998); (11c) Beer & Podsiadlowski (2002); (12) Rahoui et al. (2014); (12b) Heida et al. (2017); (13) Panizo-Espinar et al. (2021); (13b) Mata Sánchez et al. (2017); (13c) Chevalier & Ilovaisky (1991).

during the hard-intermediate state (e.g., strong asymmetries in Hα and He I–10830) and the final (low-luminosity) hard state (flat-top profiles in the Balmer and He I lines). Wind-related features are only detected in the infrared lines (e.g., blueshifted absorptions in Paβ and flat-top profiles in the Paschen and Brackett series) during the soft state. This is consistent with the results (from MAXI J1820+070) presented by Sánchez-Sierras & Muñoz-Darias (2020). They reported on the detection of infrared wind-related features during most of the outburst, whereas the optical ones were absent during the soft state. Thus, our results reinforce a scenario in which accretion disc winds are active during the whole outburst, although they are spotted at different wavelengths depending on the X-ray state. This dependence might be related to ionisation effects that make the infrared lines more sensitive to winds during the soft state (see Sánchez-Sierras & Muñoz-Darias 2020 and references therein).

4.3. On the orbital inclination

J1348 does not show dips or eclipses, which suggests it is not a high inclination system. In fact, a mid-to-low inclination is supported by the orientation of the jet ($i = 29° \pm 3°$; Carotenuto et al. 2022) assuming that there is not a strong misalignment between the jet and the orbital plane. Although our analysis is not focused on this issue, the HID (Fig. 1) supports this conclusion since it shows a squared q-shape evolution (with an almost horizontal hard-to-soft transition), a suggested property of BH LMXBs with mid-to-low inclinations (Muñoz-Darias et al. 2013).

In addition, some spectral lines, such as Hα and He I–10830 (Fig. 3), are double-peaked, which might be interpreted as a relatively high inclination feature. However, peak-to-peak separations for Hα seem to be narrower (300–600 km s^{-1}; see Sect. 3) than those measured in high inclination LMXBs (e.g., ~1900 km s^{-1} in MAXI J1659−152, Torres et al. 2021, ~1200 km s^{-1} in XTE J1118+480 Torres et al. 2002 or 500−1100 km s^{-1} in MAXI J1803−298, Mata Sánchez et al. 2022).

Overall, a mid-to-low inclination is favoured by all the available observables. This might explain the peculiar observational properties of the wind in this object. For instance, a predominantly equatorial wind would be detected with a lower (projected) velocity in a low inclination system. In addition, this would make it more difficult to form blueshifted absorptions that reach fluxes below the continuum level since the contribution from the accretion disc emission lines is larger at low velocities (i.e., as the blueshifted absorption moves closer to the core of the disc line). Therefore, unless the wind features are very strong, one might naturally expect to detect them as low velocity absorption troughs qualitatively similar to those reported in this work.

5. Summary and conclusions

We have presented OIR spectroscopy of the BH candidate MAXI J1348–630 obtained during its discovery outburst in 2019. We report the detection of several spectral features that are commonly associated with the presence of outflows. In particular, we find:

- Blueshifted absorption troughs during the SIMS (Hβ, He I–5876, Hα and Paβ) and the soft state (Paβ). They are centred at $-500\,\mathrm{km\,s^{-1}}$.
- Broad emission line wings (Hα and Paβ) reaching velocities of up to $\pm1700\,\mathrm{km\,s^{-1}}$, as well as asymmetric lines with a negative skew and flat-top profiles. They are seen at different stages of the outburst.

We interpret these features as signatures of a cold (OIR) accretion disc wind that is present during, at least, the brightest phases of the accretion episode. The apparently lower velocity of the blueshifted absorptions as compared to those seen in other LMXBs might be related to the mid-to-low orbital inclination of the system. Further spectroscopic observations of the system are encouraged during both quiescence and forthcoming outbursts in order to determine its fundamental parameters and better characterise the properties of the wind.

Acknowledgements. We are thankful to the anonymous referee for constructive comments that have improved this paper. DMS and MAP acknowledge support from the Consejería de Economía, Conocimiento y Empleo del Gobierno de Canarias and the European Regional Development Fund (ERDF) under grant with reference ProID2020010104 and ProID2021010132. TMD and MAPT acknowledge support via the Ramón y Cajal Fellowships RYC-2015-18148 and RYC-2015-17854, respectively. KIIK acknowledges funding from the European Research Council (ERC) under the European Union's Horizon 2020 research and innovation programme (grant agreement No. 101002352) and from the Academy of Finland projects 320045 and 320085. GP acknowledges funding from the European Research Council (ERC) under the European Union's Horizon 2020 research and innovation programme (grant agreement No 865637). This work has been supported in part by the Spanish Ministry of Science under grants AYA2017-83216-P, PID2020-120323GB-I00 and EUR2021-122010. MOLLY software developed by Tom Marsh is gratefully acknowledged. Based on observations collected at the European Southern Observatory under ESO programmes 0102.D-0309(A) and 0102.D-0799(A). This research has made use of MAXI data provided by RIKEN, JAXA and the MAXI team.

References

Baglio, M. C., Russell, D. M., Bramich, D., & Lewis, F. 2019, ATel, 12491, 1
Baglio, M. C., Russell, D. M., Bramich, D. M., et al. 2020, ATel, 13710, 1
Bandyopadhyay, R. M., Shahbaz, T., Charles, P. A., & Naylor, T. 1999, MNRAS, 306, 417
Beals, C. S. 1931, MNRAS, 91, 966
Beer, M. E., & Podsiadlowski, P. 2002, MNRAS, 331, 351
Belloni, T. M., Motta, S. E., & Muñoz-Darias, T. 2011, Bull. Astron. Soc. India, 39, 409
Belloni, T. M., Zhang, L., Kylafis, N. D., Reig, P., & Altamirano, D. 2020, MNRAS, 496, 4366
Buisson, D. J. K., Hare, J., Guver, T., et al. 2020, ATel, 13563, 1
Buisson, D. J., Altamirano, D., Armas Padilla, M., et al. 2021, MNRAS, 503, 5600
Buxton, M., & Vennes, S. 2003, MNRAS, 342, 105
Carotenuto, F., Corbel, S., Tremou, E., et al. 2021, MNRAS, 504, 444
Carotenuto, F., Tetarenko, A. J., & Corbel, S. 2022, MNRAS, 511, 4826
Casares, J., Charles, P. A., Jones, D. H. P., Rutten, R. G. M., & Callanan, P. J. 1991, MNRAS, 250, 712
Casares, J., Marsh, T. R., Charles, P. A., et al. 1995, MNRAS, 274, 565
Casares, J., Muñoz-Darias, T., Mata Sánchez, D., et al. 2019, MNRAS, 488, 1356
Castro Segura, N., Knigge, C., Long, K. S., et al. 2022, Nature, 603, 52
Chaty, S., Charles, P. A., Martí, J., et al. 2003, MNRAS, 343, 169
Chauhan, J., Miller-Jones, J. C., Raja, W., et al. 2021, MNRAS, 501, 60
Chevalier, C., & Ilovaisky, S. A. 1991, A&A, 251, L11
Corral-Santana, J. M., Casares, J., Muñoz-Darias, T., et al. 2013, Sci, 339, 1048
Corral-Santana, J. M., Casares, J., Munoz-Darias, T., et al. 2016, A&A, 587, A61
Cúneo, V. A., Alabarta, K., Zhang, L., et al. 2020a, MNRAS, 496, 1001
Cúneo, V. A., Muñoz-Darias, T., Sánchez-Sierras, J., et al. 2020b, MNRAS, 498, 25
Díaz Trigo, M., & Boirin, L. 2016, Astron. Nachrichten, 337, 368
Díaz Trigo, M., Sidoli, L., Boirin, L., & Parmar, A. N. 2012, A&A, 543, A50
Done, C., Gierliński, M., & Kubota, A. 2007, A&AR, 15, 1
Fender, R., & Muñoz-Darias, T. 2016, in Lect. Notes Phys., eds. F. Haardt, V. Gorini, U. Moschella, A. Treves, & M. Colpi (Cham: Springer International Publishing), 905, 65
Fender, R. P., Belloni, T. M., & Gallo, E. 2004, MNRAS, 355, 1105
Fomalont, E. B., Geldzahler, B. J., & Bradshaw, C. F. 2001, ApJ, 558, 283
Gallo, E., Fender, R. P., & Pooley, G. G. 2003, MNRAS, 344, 60
Gilfanov, M. 2010, Jet Paradig. Lect. Notes Phys., 794, 17
Gottlieb, E. W., Wright, E. L., & Liller, W. 1975, ApJ, 195, L33
Heida, M., Jonker, P. G., Torres, M. A. P., & Chiavassa, A. 2017, ApJ, 846, 132
Higginbottom, N., Knigge, C., Long, K. S., Matthews, J. H., & Parkinson, E. J. 2019, MNRAS, 484, 4635
Homan, J., Wijnands, R., van der Klis, M., et al. 2001, ApJS, 132, 377
Homan, J., Neilsen, J., Allen, J. L., et al. 2016, ApJ, 830, L5
Homan, J., Gendreau, K. C., Sanna, A., et al. 2021, ATel, 14606, 1
Iaria, R., Di Salvo, T., Burderi, L., et al. 2014, A&A, 561, A99
Jenniskens, P., & Désert, F.-X. 1994, A&AS, 106, 9
Jiménez-Ibarra, F., Muñoz-Darias, T., Casares, J., Padilla, M. A., & Corral-Santana, J. M. 2019, MNRAS, 489, 3420
Kaur, R., Kaper, L., Ellerbroek, L. E., et al. 2012, ApJ, 746, L23
Kausch, W., Noll, S., Smette, A., et al. 2015, A&A, 576, A78
Khargharia, J., Froning, C. S., & Robinson, E. L. 2010, ApJ, 716, 1105
Lamer, G., Schwope, A. D., Predehl, P., et al. 2021, A&A, 647, A7
Lindstrøm, C., Griffin, J., Kiss, L. L., et al. 2005, MNRAS, 363, 882
Macdonald, R. K., Bailyn, C. D., Buxton, M., et al. 2014, ApJ, 784, 2
Mata-Sánchez, D., Muñoz-Darias, T., Casares, J., Corral-Santana, J. M., & Shahbaz, T. 2015a, MNRAS, 454, 2199
Mata Sánchez, D., Muñoz-Darias, T., Casares, J., et al. 2015b, MNRAS, 449, L1
Mata Sánchez, D., Muñoz-Darias, T., Casares, J., & Jiménez-Ibarra, F. 2017, MNRAS, 464, L41
Mata Sánchez, D., Muñoz-Darias, T., Casares, J., et al. 2018, MNRAS, 481, 2646
Mata Sánchez, D., Muñoz-Darias, T., Cúneo, V. A., et al. 2022, ApJ, 926, L10
Matsuoka, M., Kawasaki, K., Ueno, S., et al. 2009, PASJ, 61, 999
McClintock, J. E., & Remillard, R. A. 2006, Compact Stellar X-ray Sources (Cambridge, UK: Cambridge University Press), 39, 157
Muñoz-Darias, T., Coriat, M., Plant, D. S., et al. 2013, MNRAS, 432, 1330
Muñoz-Darias, T., Fender, R. P., Motta, S. E., & Belloni, T. M. 2014, MNRAS, 443, 3270
Muñoz-Darias, T., Casares, J., Mata Sánchez, D., et al. 2016, Nature, 534, 75
Muñoz-Darias, T., Casares, J., Mata Sánchez, D., et al. 2017, MNRAS, 465, L124
Muñoz-Darias, T., Torres, M. A. P., & Garcia, M. R. 2018, MNRAS, 479, 3987
Muñoz-Darias, T., Jiménez-Ibarra, F., Panizo-Espinar, G., et al. 2019, ApJ, 879, L3
Muñoz-Darias, T., Armas Padilla, M., Jiménez-Ibarra, F., et al. 2020, ApJ, 893, L19
Nakahira, S., Kawai, N., Negoro, H., et al. 2019, ATel, 12469, 1
Negoro, H., Nakajima, M., Aoki, M., et al. 2020, ATel, 13994, 1
Neilsen, J., & Lee, J. C. 2009, Nature, 458, 481
Orosz, J. A., Kuulkers, E., van der Klis, M., et al. 2001, ApJ, 555, 489
Panizo-Espinar, G., Muñoz-Darias, T., Armas Padilla, M., et al. 2021, A&A, 650, A135
Pirbhoy, S. F., Baglio, M. C., Russell, D., et al. 2020, ATel, 13451, 1
Ponti, G., Fender, R. P., Begelman, M. C., et al. 2012, MNRAS, 422, 11
Ponti, G., Muñoz-Darias, T., & Fender, R. P. 2014, MNRAS, 444, 1829
Prinja, R. K., Fullerton, A. W., & Crowther, P. A. 1996, A&A, 311, 264
Rahoui, F., Coriat, M., & Lee, J. C. 2014, MNRAS, 442, 1610
Russell, D. M., Miller-Jones, J. C. A., Maccarone, T. J., et al. 2011, A&A, 739, L19
Russell, D. M., Baglio, C. M., Lewis, F., et al. 2019a, ATel, 12439, 1
Russell, D. M., Bramich, D. M., Lewis, F., et al. 2019b, Astron. Nachr., 340, 278
Sánchez-Sierras, J., & Muñoz-Darias, T. 2020, A&A, 640, L3
Sanna, A., Uttley, P., Altamirano, D., et al. 2019, ATel, 12447, 1
Shakura, N. I., & Sunyaev, R. A. 1973, IAU Symp., 55, 155
Smak, J. 1969, AcA, 19, 155
Smette, A., Sana, H., Noll, S., et al. 2015, A&A, 576, A77
Soria, R., Wu, K., & Hunstead, R. W. 2000, ApJ, 539, 445
Torres, M. A. P., Callanan, P. J., Garcia, M. R., et al. 2002, ApJ, 569, 423
Torres, M. A., Jonker, P. G., Miller-Jones, J. C., et al. 2015, MNRAS, 450, 4292
Torres, M. A. P., Casares, J., Jiménez-Ibarra, F., et al. 2019, ApJ, 882, L21
Torres, M. A. P., Casares, J., Jiménez-Ibarra, F., et al. 2020, ApJ, 893, L37
Torres, M. A., Jonker, P. G., Casares, J., Miller-Jones, J. C., & Steeghs, D. 2021, MNRAS, 501, 2174
Ueda, Y., Inoue, H., Tanaka, Y., et al. 1998, ApJ, 492, 782
Vainu Bappu, M. K., & Menzel, D. H. 1954, ApJ, 119, 508
van der Hooft, F., Heemskerk, M. H. M., Alberts, F., et al. 1998, A&A, 329, 538
Vernet, J., Dekker, H., D'Odorico, S., et al. 2011, A&A, 536, A105
Williams, R., & Mason, E. 2010, Ap&SS, 327, 207
Xu, Y., Harrison, F., Xu, Y., & Harrison, F. 2021, ATel, 14609, 1
Yao, Y., Kulkarni, S. R., Burdge, K. B., et al. 2021, ApJ, 920, 120
Yatabe, F., Negoro, H., Nakajima, M., et al. 2019, ATel, 12425, 1
Zhang, L., Altamirano, D., Cúneo, V. A., et al. 2020, MNRAS, 499, 851
Zhang, L., Altamirano, D., Uttley, P., et al. 2021, MNRAS, 505, 3823
Zhang, W., Tao, L., Soria, R., et al. 2022, ApJ, 927, 210